RESEARCH ARTICLE SUMMARY

NEUROSCIENCE

Astrocyte Ca^{2+}-evoked ATP release regulates myelinated axon excitability and conduction speed

Jonathan Lezmy*, I. Lorena Arancibia-Cárcamo, Tania Quintela-López, Diane L. Sherman, Peter J. Brophy, David Attwell*

INTRODUCTION: Astrocytes support neuronal function throughout the central nervous system. In the gray matter, they regulate synapse number during development, remove synaptically released neurotransmitters to terminate their action and prevent excitotoxicity, control the extracellular potassium concentration to prevent hyperexcitability, regulate blood flow to ensure an adequate energy supply, provide lactate to neurons for energy, and respond to rises of intracellular calcium concentration ([Ca^{2+}]$_i$) by releasing adenosine triphosphate (ATP) and other gliotransmitters that act on neuronal receptors to modulate information processing. However, their role is unclear in the white matter, which transmits information rapidly between gray matter areas using axons wrapped with capacitance-reducing myelin (although they have been suggested to regulate myelination during development and during normal function).

RATIONALE: Recently, it has been suggested that learning and memory may reflect not only changes in synaptic function in the gray matter, but also changes in white matter function. In particular, neural circuit function might be regulated by changes in the conduction speed of myelinated axons that result in an altered arrival time of action potentials at a distant neuron. These speed changes might be brought about by alterations of the properties of the passively conducting myelinated internodes or of the intervening excitable nodes of Ranvier, where the action potential is generated. We applied immunohistochemistry to assess how astrocytes interact with myelinated axons, neuronal stimulation and light-evoked calcium uncaging in astrocytes to evoke Ca^{2+}-dependent release of gliotransmitters, and electrophysiology and pharmacology to characterize how astrocyte-released substances might affect the axon initial segment (AIS) and nodes of Ranvier of myelinated neurons. Measurements of conduction velocity and computer modeling allowed us to interpret the results.

RESULTS: Astrocytes closely approach the axons of myelinated neurons in layer V of the cerebral cortex that enter the corpus callosum. Uncaging Ca^{2+} within astrocytes or stimulating spike trains in neurons evoked a rise of astrocyte [Ca^{2+}]$_i$ that triggered the release of ATP-containing vesicles from these cells. This evoked an inward current in the AIS and nodes of Ranvier of the pyramidal neurons. Pharmacology showed that this was mediated by the activation of G$_s$-linked adenosine A$_{2a}$ receptors (A$_{2a}$Rs), implying that the released ATP was converted to adenosine by extracellular enzymes. The A$_{2a}$Rs raise the intracellular concentration of cyclic AMP, which activates hyperpolarization-activated cyclic nucleotide–gated (HCN) channels mediating the inward hyperpolarization-activated current (I_h) and thus depolarizes the cell. In the AIS, the activation of A$_{2a}$Rs alters excitability and hence action potential generation, whereas in the nodes of Ranvier, it decreases the conduction speed of the action potential along the axon.

CONCLUSION: As in the gray matter, astrocyte [Ca^{2+}]$_i$ regulates the release of ATP into the extracellular space in the white matter. After conversion to adenosine, this regulates the excitability and conduction speed of myelinated axons. The changes in excitability at the AIS will lead to changes in the relationship between the synaptic input and action potential output of the cell. The altered conduction speed of the myelinated axon may change neural circuit function by changing the action potential arrival time at the cell's output synapses, thus altering the integration of signals in postsynaptic neurons. Variations in astrocyte-derived adenosine level can occur between wake and sleep states, and the extracellular adenosine concentration rises during energy deprivation conditions. These changes in adenosine level could thus control white matter information flow and neural circuit function. ∎

READ THE FULL ARTICLE AT
https://doi.org/10.1126/science.abh2858
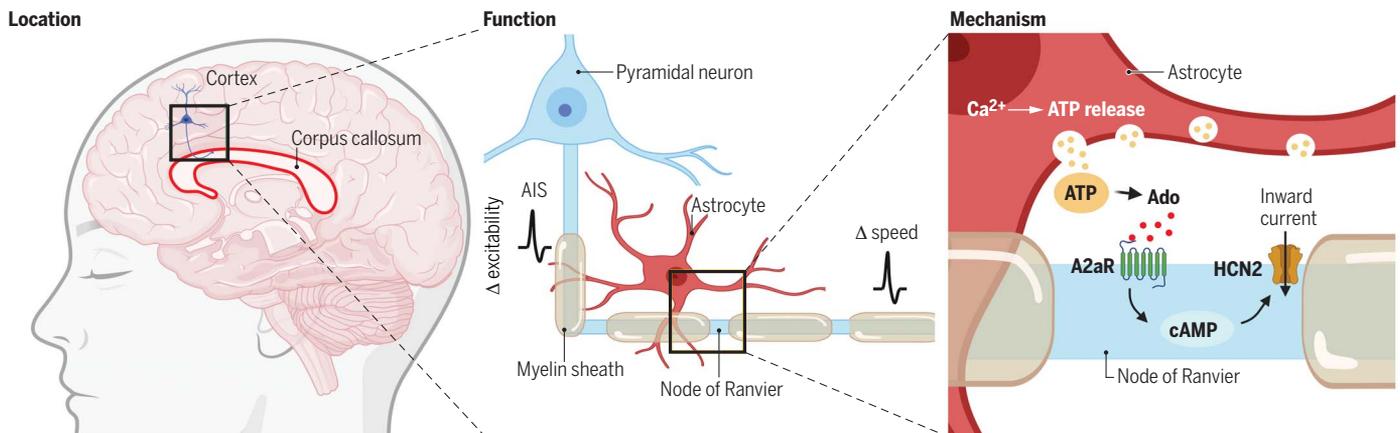
Astrocytes regulate myelinated axon excitability and conduction speed. For cortical neurons with myelinated axons crossing the corpus callosum (left), astrocytes regulate AIS excitability and axonal conduction speed (middle). Increases of astrocyte [Ca^{2+}]$_i$ release ATP, which, after conversion to adenosine (Ado) extracellularly, activates A$_{2a}$Rs that raise the intracellular cyclic AMP concentration and thus generate an inward current through HCN2 channels in the AIS and nodes of Ranvier (right). Image was created with BioRender.com.

NEUROSCIENCE

Astrocyte Ca^{2+}-evoked ATP release regulates myelinated axon excitability and conduction speed

Jonathan Lezmy[1]*, I. Lorena Arancibia-Cárcamo[1,2], Tania Quintela-López[1], Diane L. Sherman[3], Peter J. Brophy[3], David Attwell[1]*

In the brain's gray matter, astrocytes regulate synapse properties, but their role is unclear for the white matter, where myelinated axons rapidly transmit information between gray matter areas. We found that in rodents, neuronal activity raised the intracellular calcium concentration ([Ca^{2+}]$_i$) in astrocyte processes located near action potential–generating sites in the axon initial segment (AIS) and nodes of Ranvier of myelinated axons. This released adenosine triphosphate, which was converted extracellularly to adenosine and thus, through A$_{2a}$ receptors, activated HCN2-containing cation channels that regulate two aspects of myelinated axon function: excitability of the AIS and speed of action potential propagation. Variations in astrocyte-derived adenosine level between wake and sleep states or during energy deprivation could thus control white matter information flow and neural circuit function.

Astrocytes support neuronal function throughout the central nervous system. In the gray matter, they regulate synapse number during development, remove synaptically released neurotransmitters, control the extracellular [K$^+$] ([K$^+$]$_o$), regulate blood flow, and provide lactate to neurons for energy (*1*). However, their role is unclear in the white matter, which transmits information rapidly between gray matter areas using myelinated axons. Wrapping of these axons with myelin by oligodendrocytes reduces the axon capacitance and thus confers a high conduction speed for the action potential, which, once generated at the axon initial segment (AIS) (*2*), is maintained as it propagates by sodium influx at the nodes of Ranvier occurring between the myelinated internodes. Because oligodendrocytes isolate almost all of the axon from the extracellular space, they are thought to be the main mediators of [K$^+$]$_o$ control and energy provision to axons (*3*, *4*), making the role of astrocytes uncertain despite astrocyte processes occurring close to nodes of Ranvier (*5*).

Labeling for glial fibrillary acidic protein (GFAP) revealed astrocytes throughout the gray matter and white matter (Fig. 1A). On patch-clamping layer V cortical pyramidal cells or oligodendrocytes, we observed that astrocyte processes were aligned and intimately associated with the myelinated axon and its internodal sheaths (Fig. 1, B and C, and fig. S1, A to F). We used double whole-cell patch-clamping

to load an astrocyte with a Ca^{2+}-sensing dye (Fluo-4) and to depolarize a pyramidal cell to stimulate action potentials. When the pyramidal cell was driven to fire briefly (30 Hz for 1 s), the astrocyte intracellular calcium concentration ([Ca^{2+}]$_i$) rose more in processes near the neuronal dendrites [within 12.7 ± 2.5 s from start of stimulus to peak fractional change in the fluorescence signal ($\Delta F/F$); mean $\Delta F/F$ = 0.20 ± 0.03, n = 5 neuron-astrocyte pairs] than in processes near the axon ($\Delta F/F$ = 0.03 ± 0.02, P = 0.023; Fig. 1E). However, if prolonged spiking was evoked (10 s), [Ca^{2+}]$_i$ rose in both locations (Fig. 1, D and E, and movie S1; $\Delta F/F$ = 0.19 ± 0.08 and 0.17 ± 0.05, respectively, P = 0.63, n = 3). Uncaging Ca^{2+} in the astrocyte soma also raised astrocyte [Ca^{2+}]$_i$ (Fig. 1F, $\Delta F/F$ = 1.06 ± 0.51 near dendrite, $\Delta F/F$ = 1.05 ± 0.53 near axon, P = 0.86, n = 6), and neuronal activity evoked a further [Ca^{2+}]$_i$ rise superimposed on this ($\Delta F/F$ = 0.39 ± 0.09 near dendrite, $\Delta F/F$ = 0.01 ± 0.06 near axon, P = 0.018).

In the gray matter, astrocytes can modulate neuronal function by releasing adenosine triphosphate (ATP) (*6*). We imaged putative vesicles containing ATP in astrocytes around myelinated axons of layer V pyramidal neurons using quinacrine (*7*). Uncaging Ca^{2+} in the astrocyte soma evoked a Ca^{2+} wave that propagated into processes along the axon (movie S2) and triggered the loss of 43% of quinacrine-labeled vesicles (Fig. 1, G to I; P = 0.0053), a loss that was not seen when the two-photon uncaging excitation was insufficient (see the materials and methods, fig. S2) to evoke a detectable rise of [Ca^{2+}]$_i$ nor when assessing ATP vesicle number in areas 5 μm away (Fig. 1, J and K). The resulting ATP release into the extracellular solution was detected using luciferin-luciferase (see the materials and methods). Puffing 1 mM

ATP, but not artificial cerebrospinal fluid (aCSF) from a pipette into the sensing solution evoked a large increase of luciferin luminescence (Fig. 2A), and uncaging Ca^{2+} in an astrocyte soma evoked a similar response that was not seen when the uncaging illumination was too weak to evoke a detectable [Ca^{2+}]$_i$ rise (Fig. 2, B and C).

On release, ATP is rapidly hydrolyzed to adenosine by ecto–adenosine triphosphatases (ecto-ATPases) located on microglia and astrocytes (*8*). Microglia and astrocytes associate with both the AIS and nodes of Ranvier (*9*, *10*). Adenosine receptors have previously been reported at synapses. We used immunohistochemistry to identify adenosine receptors on layer V neuron myelinated axons. Neither A$_1$ nor A$_{2b}$ receptors were detected (fig. S1, G and H), but A$_{2a}$ receptors (A$_{2a}$Rs) were found at 92% of AISs (Fig. 2D, E and H) and at 85% of nodes of Ranvier (Fig. 2, F to H). Overview images of the cortex (fig. S3D) showed A$_{2a}$R–expressing AISs leading toward the corpus callosum, implying that these were excitatory neurons. A$_{2a}$Rs were detected in fewer nodes of the cerebellar white matter, which contains excitatory mossy and climbing fiber axons as well as inhibitory Purkinje cell axons (70%; fig. S3F), and were absent from AISs of cerebellar Purkinje cells (fig. S3E), implying a neuron type–specific expression of A$_{2a}$Rs in myelinated axons. A$_{2a}$Rs raise the cyclic AMP level, which can affect cell excitability by promoting the opening of the hyperpolarization-activated cyclic nucleotide–gated (HCN) type channels (*11*, *12*) present in axons (*13*–*15*). We detected HCN2 channel subunits at 51% of AISs and at 64% of nodes of Ranvier (Fig. 2, I to M). HCN1 subunits were observed in pyramidal cell somata and in nodes of Ranvier (fig. S1, G to I). Adenosine receptors and HCN channels have not previously been reported at the node of Ranvier.

To examine the effect of activation of these A$_{2a}$Rs, we patch-clamped layer V pyramidal neurons and applied adenosine (100 μM from a puffer pipette) or another agonist for A$_{2a}$Rs (CGS 21680, 0.5 μM) to the AIS (Fig. 3A). Activating A$_{2a}$Rs in this way depolarized the cell by 6 to 7 mV (Fig. 3, A, B, and E; aCSF had no effect). The action potential response to small injected currents was increased in frequency (Fig. 3, C, F, and G), but at high injected currents was reduced, presumably as a result of increased Na$^+$ channel inactivation (Fig. 3, D, F, and H). Hyperpolarizing the cell evoked a time-dependent inward current increase (Fig. 3I), which was mediated by I_h (HCN) channels, because it was blocked by the I_h blocker ZD7288 (fig. S4). Applying CGS 21680 increased the amplitude of I_h tail currents, reflecting an increase in magnitude of the fully activated conductance of 51% in 6 cells (P = 0.029), and shifted the 50% point of the activation curve derived from these

[1]Department of Neuroscience, Physiology and Pharmacology, University College London, London WC1E 6BT, UK. [2]UK Dementia Research Institute, Francis Crick Institute, London NW1 1AT, UK. [3]Centre for Discovery Brain Sciences, University of Edinburgh, Edinburgh EH16 4SB, UK.
*Corresponding author. Email: j.lezmy@ucl.ac.uk (J.L.); d.attwell@ucl.ac.uk (D.A.)
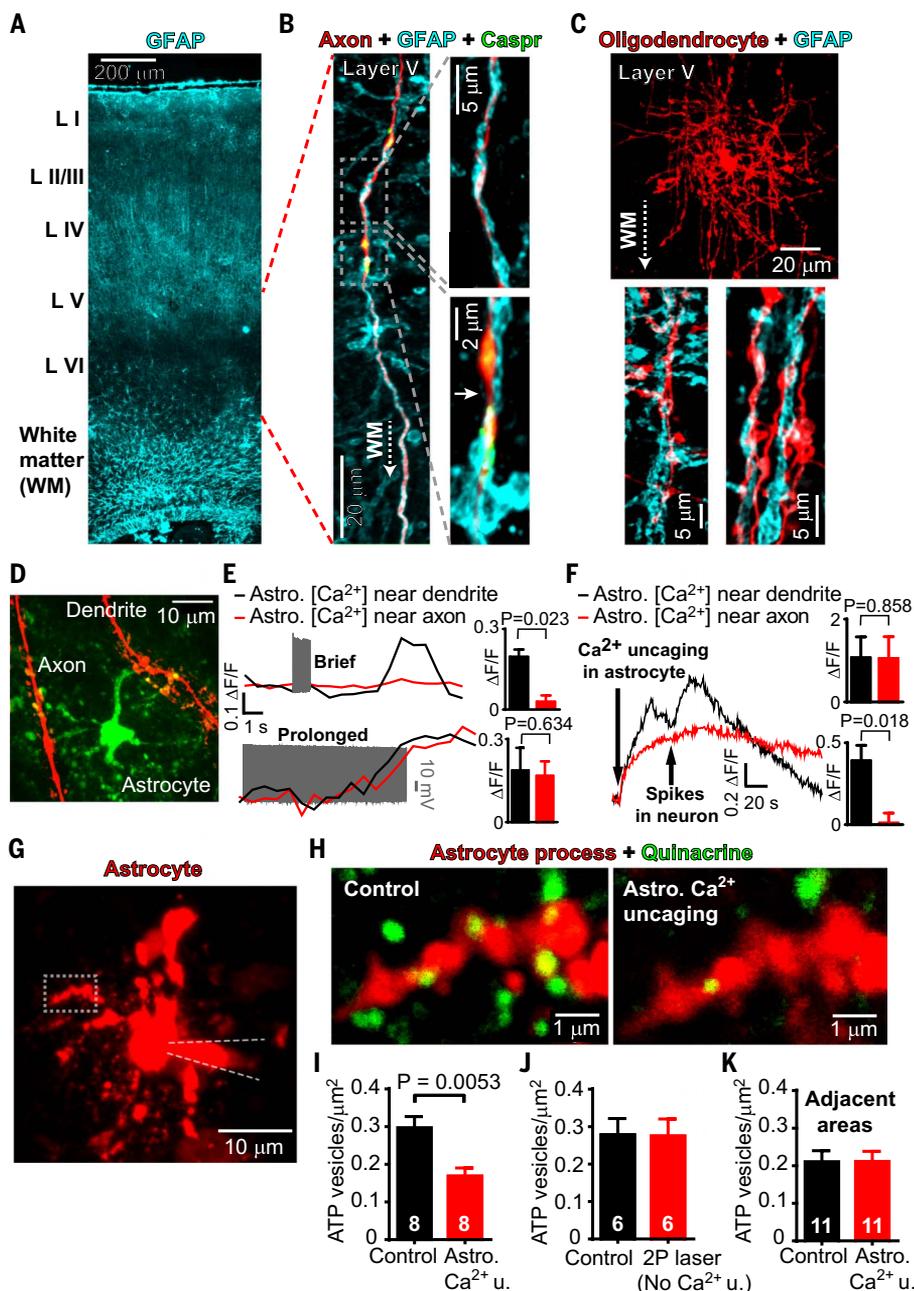
Fig. 1. Astrocyte processes near myelinated axons release ATP in response to [Ca²⁺]ᵢ rises. (**A**) GFAP labeling of mouse coronal slice showing astrocytes in gray matter and white matter. (**B**) Patch-clamp–loaded Alexa Fluor 594 labels axon of layer V pyramidal cell. Expanded internodal (top) and nodal (bottom, identified by Caspr labeling, node is at arrow) regions reveal astrocytes at both locations. (**C**) Patch-clamped oligodendrocyte in layer V with insets below showing GFAP labeling around myelinated internodes. (**D**) Dendrite and axon of patch-clamped rat layer V pyramidal cell near an astrocyte loaded with the Ca²⁺ sensor Fluo-4. (**E**) [Ca²⁺]ᵢ response in astrocyte processes near dendrite (black) and axon (red) to neuron depolarization with 500 pA for 1 s (top, n = 5) or 10 s (bottom, n = 3) to evoke spiking (gray). (**F**) [Ca²⁺]ᵢ response in astrocyte processes to Ca²⁺ uncaging and to brief neuronal spike trains (n = 6). Top bar chart shows the Ca²⁺ response just before spiking; bottom bar chart shows Ca²⁺ response after neuron spiking evoked by 500 pA for 1 s. (**G**) Patch-clamped rat astrocyte loaded with Ca²⁺ cage NP-EGTA and Rhod-2 to measure [Ca²⁺]ᵢ; the region imaged for (H) is shown. (**H**) Quinacrine-labeled puncta in astrocyte process are depleted on uncaging Ca²⁺ (Rhod 2 may not enter the smallest astrocyte processes, explaining why some puncta appear outside the astrocyte). (**I** to **K**) Quantification of ATP vesicles present per square micrometer of astrocyte process before and after uncaging [Astro. Ca²⁺ u.] (I); before and after excitation that did not evoke a [Ca²⁺]ᵢ rise in the astrocyte [No Ca²⁺ u.; see fig. S2] (J); and in regions outside the astrocyte (5 μm away) before and after uncaging (K). Numbers of processes shown on bars. Processes came from 12 cells. Data shown in (A) to (C) are from mice; those in (D) to (K) are from rats.

currents in the depolarizing direction by +8.2 mV (*P* = 0.045) so that more I_h is activated in the physiological range (Fig. 3, I to K). This shift was mimicked by including 50 μM cAMP in the patch pipette (shifted by +8.6 mV in 6 cells, *P* = 0.026), and in these cells, CGS 21680 evoked no further depolarizing shift (–1.77 mV in 6 cells, *P* = 0.087; Fig. 3, J to L).

To assess the function of A_{2a}Rs at the nodes of Ranvier, we patch-clamped layer V pyramidal cells. Dye filling revealed an enlarged bleb at the end of the axon where it was cut during the brain-slicing process. This allowed patch-clamping of the bleb (see the materials and methods), which was ~3 (mean 3.2 ± 0.4 in 5 cells) nodes away from the soma (Fig. 4A). In Thy1-Caspr-GFP mice, the nodes of layer V pyramidal neurons could be seen during the experiment, from paranodal GFP fluorescence and because axon branches often occur at nodes, and postrecording immunohistochemistry revealed A_{2a}Rs at the AIS and nodes (Fig. 4A). Puffing CGS 21680 onto a node (Fig. 4A) did not significantly depolarize the pyramidal cell soma (0.99 ± 0.46 mV in 5 cells, *P* = 0.1), implying that the puffed drug did not reach the soma or AIS. Injecting current (500 pA for 5 msec, repeated at 2 Hz) into the soma evoked an action potential. This evoked a delayed action potential in the axonal bleb, which became more delayed when CGS 21680 was puffed at an intervening node (Fig. 4B; >100 responses were averaged). Plots of rate of change of signal (d(signal)/d*t*) versus signal (Fig. 4C) were used to estimate when the action potentials in each location showed an accelerating onset phase (soma depolarization >1 mV/msec and a bleb inward current increase more negative than –0.5 pA/msec, shown as dashed lines in Fig. 4B). The latency of the response at the bleb increased from 108 ± 31 μsec in control conditions to 320 ± 89 μsec when CGS 21680 was puffed (*P* = 0.03, paired *t* test, *n* = 5 cells; Fig. 4D) and the spike width recorded at the bleb increased by 0.28 msec from 0.30 ± 0.10 msec to 0.58 ± 0.14 msec (*P* = 0.015, paired *t* test, *n* = 5).

To convert this latency increase to a change of conduction speed, we need to assume where in the AIS the action potential is initiated and how fast it propagates backward to the soma compared with forward to the bleb (see the materials and methods). If the spike starts at the middle of the AIS and the forward speed is twice the backward speed (*16*), then CGS 21680 reduced the forward speed from 1.21 ± 0.23 to 0.43 ± 0.08 m/sec (64% reduction; filled circles in Fig. 4E). Alternatively, if the spike starts at the end of the AIS and the forward speed is three times faster than the backward speed (*16*), then the speed is reduced from 0.68 ± 0.16 to 0.31 ± 0.13 m/sec (54% reduction; open circles in Fig. 4E). Thus, for a range of assumptions, activation of nodal A_{2a}Rs produces
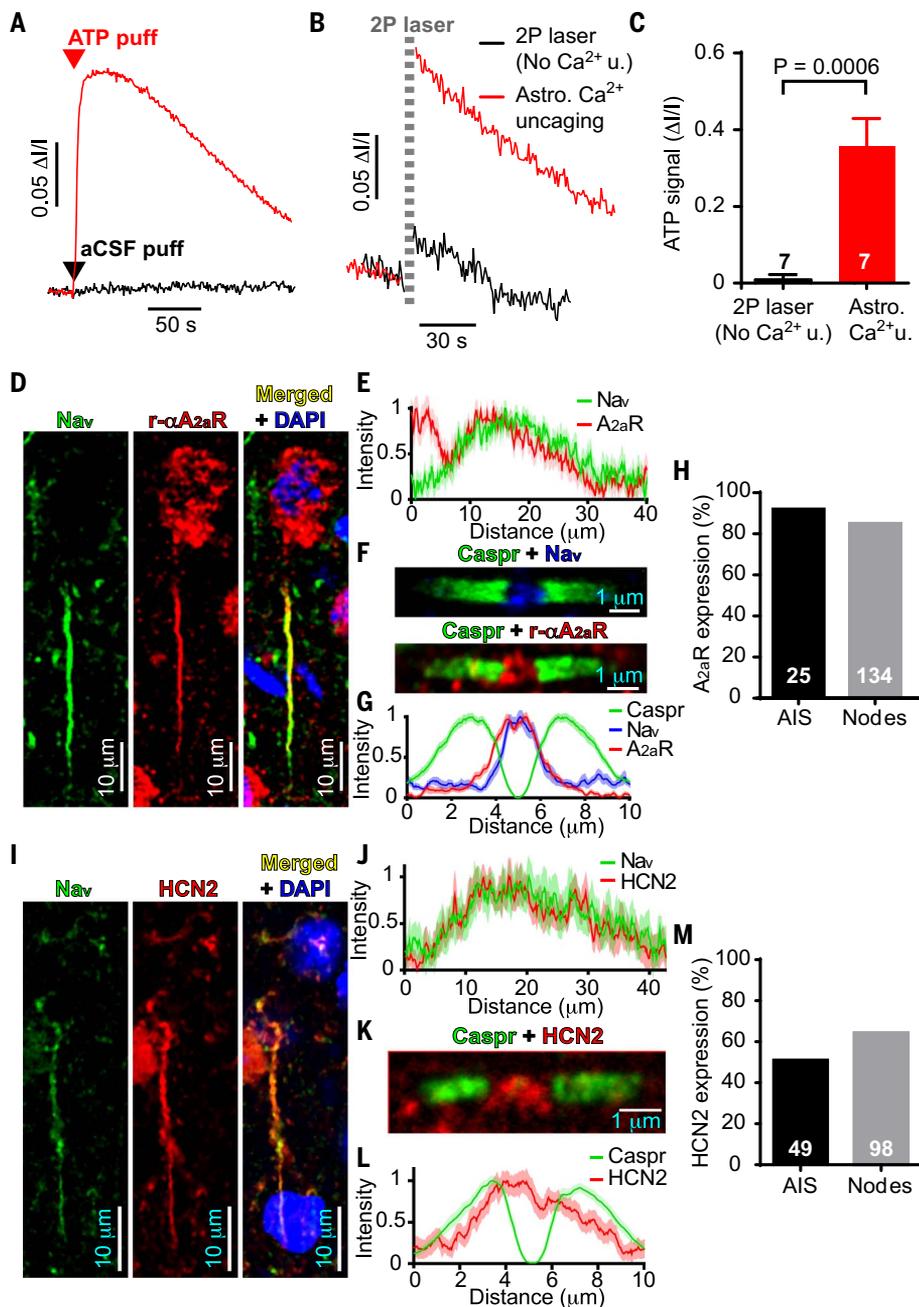
Fig. 2. ATP release from astrocytes may target adenosine receptors on myelinated axons of layer V pyramidal neurons. (**A**) Detection of ATP puffed into extracellular solution using luciferin-luciferase. (**B**) Two-photon excitation uncaging Ca^{2+} in astrocytes evoked a luciferin-luciferase signal, unless the excitation failed to raise astrocyte $[Ca^{2+}]_i$ (No Ca^{2+} u.; see fig. S2). (**C**) Quantification of experiments in (B) in seven cells. (**D** to **H**) A_{2a}Rs are present in the AIS (D), where they overlap with Na_v expression [mean of 14 Na_v and 25 A_{2a}R profiles (E)] and at the node of Ranvier (F), where they overlap with Na_v and are flanked by Caspr labeling [mean of 48 Caspr, 48 A_{2a}R and 24 Na_v profiles (G)]. (H) Percentage of 25 AISs and 134 nodes that express A_{2a}Rs. (**I** to **M**) HCN2 channel subunits are present in the AIS (I), where they overlap with Na_v expression [mean of 19 Na_v and 16 HCN2 profiles (J)], and at the node of Ranvier (K), where they overlap with Na_v and are flanked by Caspr labeling [mean of 53 Caspr and HCN2 profiles (L)]. (M) Percentage of 49 AISs and 98 nodes that express HCN2. Data shown in (A) to (E), (I), and (J) are from rats; those in (F), (G), (K), and (L) are from mice; and those in (H) and (M) combine rat AIS and mouse node data.

a very significant reduction of conduction velocity ($P = 0.0017$ comparing the ratio of the conduction velocities).

To explore how A_{2a}Rs and I_h affect excitability and conduction velocity, we used a MATLAB model of myelinated axons in the corpus callosum (*17*), which was adapted to mimic either (i) a soma attached to a truncated axon with three internodes and a terminal bleb (Fig. 5A) or (ii) an infinitely long axon (see the materials and methods). The AIS and nodes of Ranvier contained voltage-gated Na^+ and K^+ channels to generate action potentials, whereas the soma and bleb lacked these channels. We modeled the I_h current in the absence of A_{2a}R activation as being present in the soma and proximal AIS only and unaffected by the puff application of A_{2a}R-activating drugs at the distal AIS (and the [cAMP] rise that they produce), consistent with the presence in the somatodendritic compartment (fig. S1G) of I_h channels composed of HCN1 subunits (*18*), which are relatively insensitive to cAMP (*19*). The increase in I_h evoked by A_{2a}R activation in the AIS was modeled as the addition of an extra current mediated by cAMP-activated HCN2 channels located in the distal AIS. The maximum conductance of this extra current was set to increase the total maximum I_h conductance (measured at the soma) by 51% as observed (Fig. 3I), and the midpoint of the activation curve was set at –80 mV to reproduce the positive shift for the total I_h apparent activation curve in Fig. 3J. Adenosine-activated I_h was also added to the nodes of Ranvier at a density 1.41-fold higher than in the distal AIS, as measured immunohistochemically (see the materials and methods).

Adding the adenosine-activated conductance to the distal AIS in the model depolarized the soma by 5.9 mV, as seen experimentally (Figs. 3E and 5B). It also increased the firing evoked by a small injected current (Fig. 5, C and D) while decreasing that evoked by a large current (Fig. 5, C and D), also as seen experimentally (Fig. 3, C to H). However, the simulated depression of action potential amplitude at large currents was larger than that observed experimentally. These changes were largely a result of the I_h added to the AIS, because adding it solely to the nodes had only a minor effect on the resting potential at the soma (Fig. 5B). Adding I_h to the nodes of Ranvier decreased the conduction speed (Fig. 5E), as observed when puffing CGS 21680 onto the nodes (Fig. 4E). The predicted reduction was smaller than that observed experimentally, presumably because of the mild depolarization generated at the nodes (+3.8 mV). Using the infinite cable model, adding the adenosine-activated I_h depolarized the nodes by +11.4 mV, reduced the predicted conduction speed by 48% from 2.23 to 1.17 m/s (Fig. 5F), and increased the axonal spike width by 0.22 ms (mainly by increasing
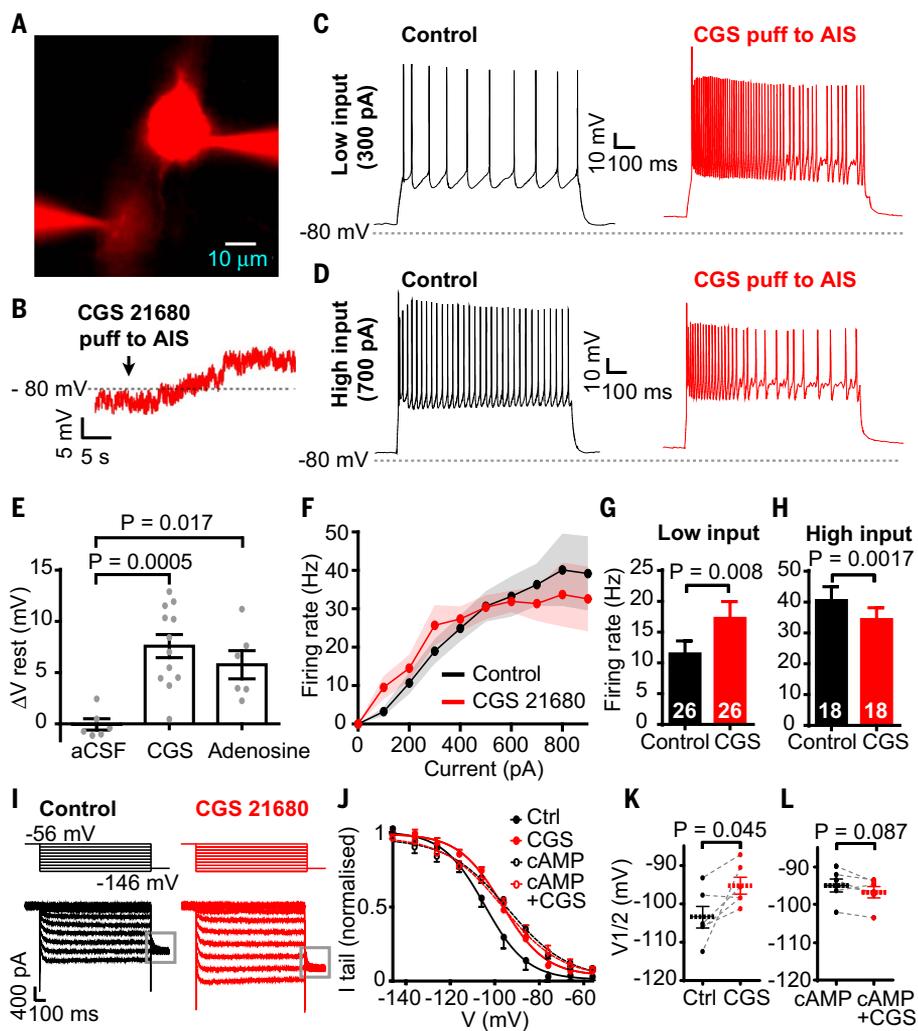
Fig. 3. A$_{2a}$ receptors, through cAMP and I_h, modulate excitability at the AIS. (**A**) Patch-clamped layer V pyramidal cells loaded with Alexa Fluor 594. Lower pipette puffing adenosine at distal AIS contains Alexa Fluor 594 to delineate the region affected by adenosine. (**B**) Depolarization of soma evoked by puffing the A$_{2a}$R agonist CGS 21680 (0.5 µM). (**C** and **D**) Voltage response to 300 pA (C) or 700 pA (D) injected current with and without CGS 21680 application. (**E**) Mean resting potential change when puffing aCSF (n = 6), 0.5 µM CGS 21680 (n = 12), or 100 µM adenosine (n = 6) onto the AIS. (**F**) Firing rate averaged over 1 s as a function of injected current, in control conditions or with CGS 21680 applied to the AIS (n = 9; SEM shown faint). (**G** and **H**) Firing rate change for "low" [averaged over 100 to 300 pA, 26 current steps from nine cells (G)] or "high" (700 to 900 pA, 18 current steps from eight cells (H)] input currents. (**I**) Specimen currents on stepping from −56 mV to various pulse potentials and then to −136 mV to evoke tail currents, allowing construction of the activation curve in control conditions and with CGS 21680 puffed at the AIS. (**J**) I_h activation curves for normal conditions, puff application of CGS 21680 (n = 6), and both with 50 µM cAMP included in the patch pipette (n = 6). (**K**) $V_{1/2}$ values (50% activation voltage of fitted Boltzmann curve) before (Ctrl) and during CGS 21680 application. (**L**) As in (K) but with cAMP in patch pipette. All data are from rats.

Na$^+$ channel inactivation at the resting potential because this was mimicked by decreasing the peak Na$^+$ conductance ~twofold), similar to the 0.28 msec reported experimentally above.

Because astrocyte [Ca^{2+}]$_i$ rises evoked the release of ATP (Fig. 1, G to K, and Fig. 2, A to C), which is expected to be converted to adenosine extracellularly and to act on A$_{2a}$Rs at the AIS and nodes of Ranvier, we tested whether

uncaging Ca^{2+} in astrocytes modulated the excitability and conduction speed of cortical layer V pyramidal cell myelinated axons. Ca^{2+} was uncaged in an astrocyte with processes running near the AIS of a pyramidal cell (Fig. 6A and movie S3). Within 70 s of uncaging the Ca^{2+}, the resting potential of the neuron was depolarized (Fig. 6B) and the action potential response of the neuron was changed (Fig. 6C),

exhibiting a higher firing rate to low injected currents (P = 0.0175 when comparing firing rates normalized to the maximum rate evoked at high injected current) and a lower firing rate to high injected currents (P = 0.0136). These changes, which are similar to those seen when activating AIS A$_{2a}$Rs (Fig. 3, B to H), were not mediated by glutamate release from astrocytes (fig. S5), were blocked by superfusion of the A$_{2a}$R blocker ZM 241385 (100 nM) or by intracellular dialysis of the neuron with the I_h blocker ZD7288 (20 µM), and were not seen if the uncaging illumination failed to evoke a [Ca^{2+}]$_i$ rise (Fig. 6, B to F).

Uncaging Ca^{2+} in astrocytes, which were shown by post hoc immunostaining to have processes close to nodes of Ranvier (Fig. 6, G and H), evoked a decrease of axonal conduction speed (Fig. 6I) in experiments monitoring the action potential propagation from the soma to a bleb ~4 (mean 3.8 ± 0.5 in 5 cells) nodes along the axon. These data are similar to those obtained by puffing an A$_{2a}$R agonist onto the nodes (Fig. 4) and, as for those experiments, the decrease of conduction speed calculated was dependent on the exact site of action potential initiation within the AIS and its forward and backward propagation speeds (Fig. 6I). Introducing ZD7288 (20 µM) into the targeted axons to block I_h (HCN) channels prevented the speed reduction evoked by astrocyte Ca^{2+} activity (fig. S6A). In unmyelinated axons and some other neuronal types, axonal HCN channels can speed, rather than slow, the action potential ([13], [14]) (see fig. S6 legend). Inducing robust neuronal activity (30 Hz for 1 min) to raise astrocyte [Ca^{2+}]$_i$ (Fig. 1E) also induced a decrease of axonal conduction speed (P = 0.014), which was abolished by superfusing the A$_{2a}$R blocker ZM 241385 (100 nM) (fig. S6B).

These data reveal a new modulation of neuronal circuit function by glial cells. Astrocyte modulation of neuronal synaptic function in the gray matter has been accepted as a major determinant of neuronal function ([6], [20], [21]), but the role of white matter astrocytes is less clear. Our data, summarized in fig. S7, demonstrate that astrocytes modulate the excitability of the AIS of excitatory neurons and regulate the conduction speed of myelinated axons. This regulation is a result of astrocytes raising the concentration of adenosine near the AIS or nodes of Ranvier (of a single axon or possibly several axons at once), which can increase or decrease AIS excitability and decreases axon conduction speed. Adenosine release can occur when axonal action potential firing raises [Ca^{2+}]$_i$ in adjacent astrocytes ([22]); this triggers the release of ATP from vesicles (Figs. 1 and 2), which is subsequently converted to adenosine by ecto-ATPases expressed by microglia, astrocytes, and oligodendrocyte lineage cells ([8]). Neuronal activity in cortical layer V
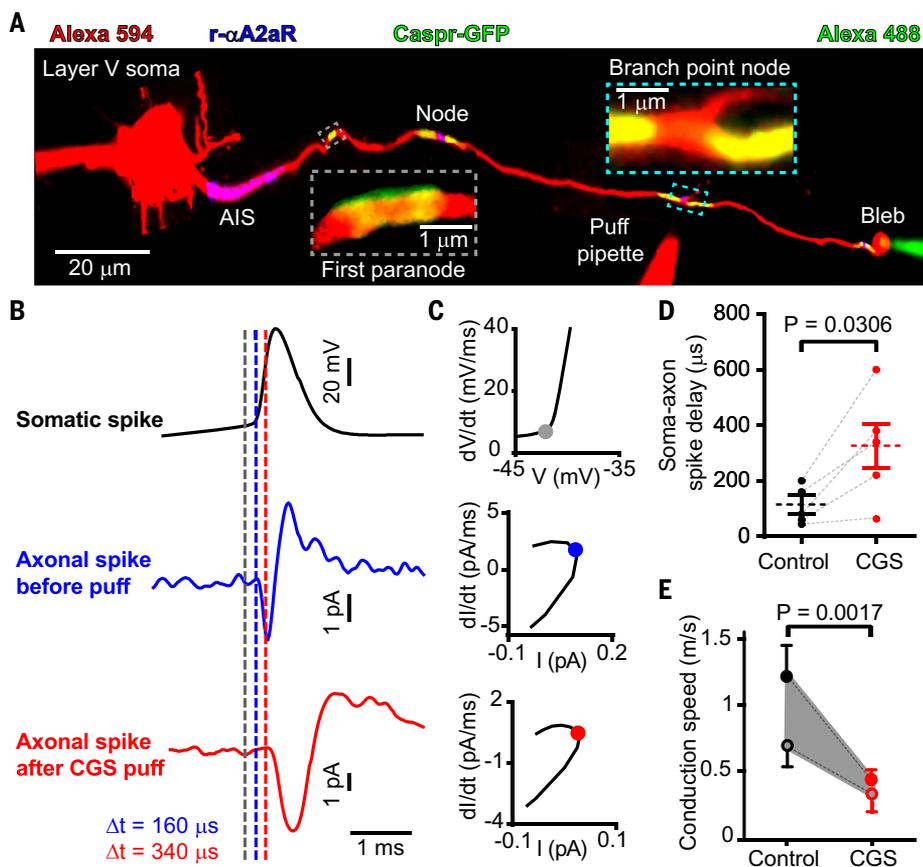
Fig. 4. A$_{2a}$Rs in the node of Ranvier modulate conduction velocity. (**A**) Myelinated axon in Thy1-Caspr-GFP mouse filled with Alexa Fluor 594 and patch-clamped at the cell soma and end-of-axon bleb. (**B**) Average of >100 evoked action potentials in the soma and bleb in control conditions and while puffing 0.5 μM CGS 21680 at a node of Ranvier. Dashed lines show times of initiation of action potential derived from threshold values of rate of change of voltage (dV/dt) or current (dI/dt) with time (see text). (**C**) Phase plane plots showing times indicated in (B) (dots). (**D**) Response latency in bleb. (**E**) Conduction velocities derived making assumptions discussed in the main text (closed circles assume spike starts at the middle of the AIS and the forward speed is twice the backward speed; open circles assume spike starts at the end of the AIS and the forward speed is three times faster than the backward speed). Data in (A) to (C) are from mice; those in (D) and (E) combine data from rats and mice (neither the initial speed nor the percentage change evoked by CGS 21680 differed significantly between rats and mice, P = 0.43 and 0.15, respectively).

gray matter readily raised [Ca^{2+}]$_i$ in astrocyte processes near neuronal dendrites, presumably as a result of classical neurotransmitters or other signaling molecules acting on astrocytes, but more intense neuronal activity (or conceivably a large number of neurons firing at a low rate) was needed to raise it in the processes near axons (Fig. 1, E and F). Thus, the overall level of neuronal activity may modulate the conduction speed of white matter axons.

Changes in the ATP level in astrocytes or neurons may also alter the extracellular adenosine concentration as a result of intracellular interconversion of ATP and adenosine and export or import of adenosine across the cell membrane by the equilibrative nucleoside transporter. Across a wide area of neocortex, the intracellular ATP level decreases during

neuronal activity, on passing from the awake state to non–rapid eye movement (non-REM) sleep, and on passing from non-REM sleep to REM sleep (23). In the basal forebrain, the accumulation of extracellular adenosine when awake has been proposed to generate pressure to sleep (24), and this adenosine is likely to be generated from ATP released by astrocytes (25, 26). Although the arousal-modulating effects of adenosine have often been attributed to it acting on presynaptic A$_1$ receptors to suppress glutamate release at excitatory synapses, genetic evidence suggests that in fact these effects are generated by A$_{2a}$Rs (27). Thus, the effects of astrocyte-derived adenosine on AIS excitability and myelinated axon conduction speed that we have characterized may be crucial contributors to mediating changes between wake and sleep states.

GABA, dopamine, and serotonin receptors regulate neuronal excitability at the AIS (15, 28, 29). Our data demonstrate that the node of Ranvier can have its electrical function rapidly altered by substances released from surrounding cells. We have shown this for astrocyte-released ATP/adenosine, but oligodendrocyte precursor cells and microglia could theoretically exert similar effects either by releasing ATP or adenosine directly onto spike generation sites or by responding to astrocytic ATP release by releasing other gliotransmitters onto the axons. Neural circuits depend crucially on action potential arrival time for their function (30), and cognition depends on oscillations of neural firing probability that in turn depend on propagation time in myelinated neurons (31–33). Thus, the decrease of the conduction speed of myelinated axons that is evoked by adenosine may change information processing and cognition, when the adenosine level rises either during a prolonged awake period or in response to complex motor behavior and pathological conditions. Indeed, behavioral effects linked to exploratory activity, aggression and anxiety (34, 35), and pathological effects in epilepsy, Parkinson's disease, Alzheimer's disease, depression, and autism have all been linked to impairments of adenosine signaling (36, 37). Our results make the testable prediction that, when adenosine levels rise during prolonged wakefulness or in complex motor behavior and pathological conditions, the conduction speed of myelinated axons should decrease, resulting in delays to the action potential arrival time at downstream synapses and possible impairments of coincidence detection or oscillatory firing generation.

Materials and Methods
Animals

Acute brain slice preparation

Coronal cortical slices (300 μm thick) were prepared on a vibratome in ice-cold solution containing (in mM): 93 N-methyl-D-glucamine
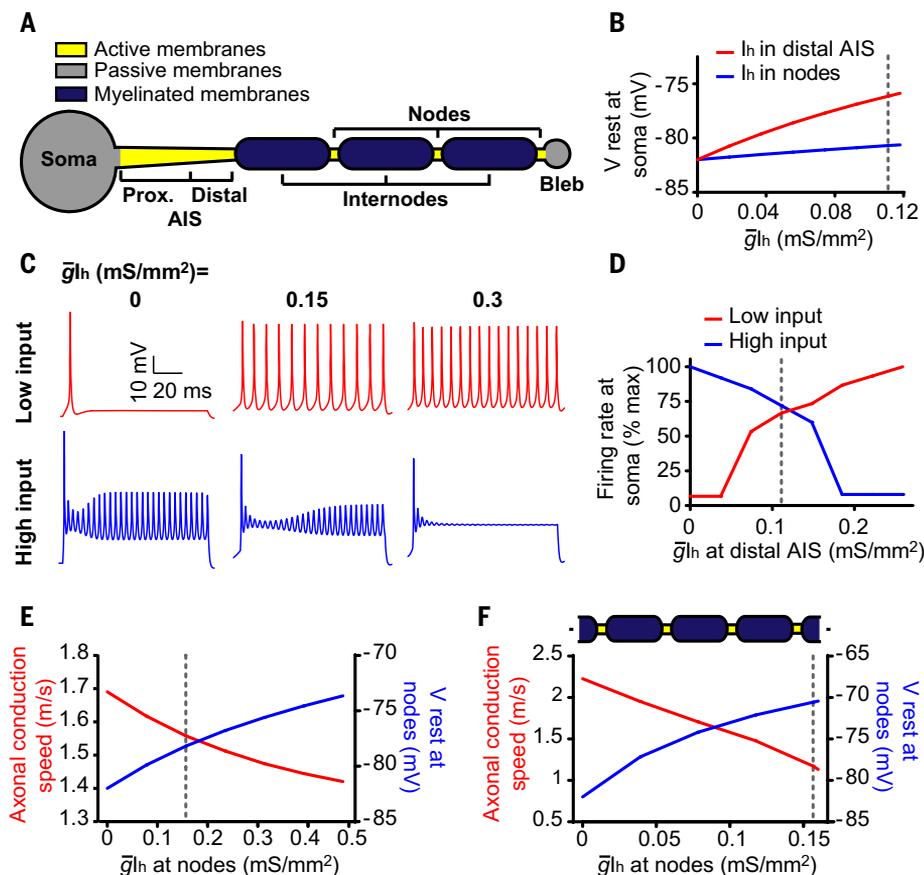
Fig. 5. Computational modeling predicts the adenosine-evoked decrease of axonal conduction speed.
(**A**) Schematic diagram of the model of the experiment in Fig. 4. (**B**) Adding different densities of adenosine-sensitive maximal I_h conductance ($\bar{g}_{lh}$) to the distal AIS evokes a larger soma depolarization than adding it to the nodes of Ranvier. Vertical dashed line shows measured maximal conductance (0.11 mS/mm²). (**C**) Voltage response at soma to injecting 20 pA (top row) or 180 pA (bottom row) with three different levels of $\bar{g}_{lh}$ added (as indicated) to the distal AIS. As observed experimentally (Fig. 3, C to H), at low injected current, the action potential frequency is increased; at high injected current, it is decreased (because of the simulated decrease of action potential amplitude, we defined an action potential as occurring if the voltage crossed −50 mV). (**D**) Firing rate as a function of $\bar{g}_{lh}$ for simulations as in (C). (**E**) Action potential speed from the first to the last node in (A) and average resting potential of the three nodes as a function of $\bar{g}_{lh}$ added to each node (vertical dashed line shows the estimated physiological value of 0.1565 mS/mm²; see the materials and methods). (**F**) Predictions of infinite axon model for conduction speed and node resting potential as a function of $\bar{g}_{lh}$.

(NMDG) chloride, 2.5 KCl, 30 NaHCO₃, 10 MgCl₂, 1.2 NaH₂PO₄, 25 glucose, 0.5 CaCl₂, 20 HEPES, 5 sodium ascorbate, 3 sodium pyruvate, and 1 kynurenic acid. The slices were incubated at 37°C in this solution for 20 min, then transferred to a similar solution containing (in mM): 93 NaCl, 1 MgCl₂, and 2 CaCl₂ instead of the NMDG chloride, MgCl₂, and CaCl₂, and incubated at room temperature until use. Experiments were performed in aCSF containing (in mM) 125 NaCl, 3 KCl, 26 NaHCO₃, 2 MgCl₂, 2 CaCl₂, 1.25 NaH₂PO₄, and 10 glucose heated to 37°C. All the solutions were gassed with 95% O₂ and 5% CO₂. In some experiments, 50 μM ZD7288, 100 nM ZM 241385, 20 μM D-AP5, 10 μM DNQX, 50 μM MSPG, and 1 μM NPS 2390 (all from Tocris Bioscience) were added to the aCSF.

Patch-clamping of neuronal somata
Experiments were performed with an Olympus BX51WI microscope under an Olympus LUMPlanFI 40× lens. Layer V pyramidal cells were identified by their location and morphology. Microelectrodes with resistances of 5 to 6 MΩ were pulled from borosilicate glass capillaries (Harvard Apparatus) and filled with an intracellular solution containing (in mM): 145 K-gluconate, 2 MgCl₂, 0.5 H₂-EGTA, 2 MgATP, 0.2 Na₂GTP, and 10 HEPES, pH adjusted to 7.2 with KOH. Somata were patch-clamped in whole-cell configuration, and the signals were amplified using a Multiclamp 700B (Molecular Devices), filtered at 4 kHz, and digitized at 50 kHz. The series resistance was <20 MΩ, was compensated by ≥70%, and did not vary by >10% during experiments. The mean input

resistance in whole-cell mode, after compensation for series resistance, was 130.6 ± 25.9 MΩ in control conditions and 84.8 ± 23.8 MΩ during CGS 21680 application to the AIS ($n = 6$, $P = 0.049$). Recordings were acquired with Clampex and analyzed with Clampfit software (Molecular Devices). In current-clamp mode, bridge balance and pipette capacitance were corrected. To generate graphs of firing rate versus injected current, current steps in increments of 100 pA were injected for 1 s. All membrane potentials were corrected for a pipette liquid junction potential of −16 mV. To analyze currents activated by hyperpolarization, tail currents were analyzed at −136 mV obtained after 1 s pretest pulses in 10-mV increments from −56 to −146 mV. The tail currents analyzed were primarily generated by HCN channels (I_h current) because they were significantly diminished by adding 50 μM ZD7288 (Tocris Bioscience) (fig. S4). Tail currents were fitted with single exponential curves that were extrapolated back to the end of the pretest pulses. The resulting tail amplitude values were fit to a function:

$$I = I_{max} + (I_{min} - I_{max})/\{1 + \exp[k(V - V_{1/2})]\} \quad (1)$$

where I_{max} is the predicted tail amplitude at −136 mV for a large depolarizing voltage step, I_{min} is the tail amplitude for a large hyperpolarizing step, $V_{1/2}$ is the voltage midpoint of the activation curve, and k is a factor defining the slope of the activation curve. The conductance conferred by the maximally activated current is given by

$$G_{max} = (I_{max} - I_{min})/[V_{rev} - (-136 \text{ mV})] \quad (2)$$

where the reversal potential of I_h was taken as −23 mV (13). In some experiments, 50 μM cAMP (Sigma-Aldrich) or 20 μM ZD7288 (Tocris Bioscience) was added to the intracellular solution. ZD7288 was previously shown to block I_h when applied intracellularly (15).

Patch-clamp recording from axonal blebs
Experiments were performed using a Zeiss LSM780 two-photon confocal microscope with a W Plan-Apochromat 20× objective. Blebs are patchable structures formed at the cut end of axons at the surface of slices (39). Alexa Fluor 594 (ThermoFisher Scientific) was allowed time to diffuse from the soma to the bleb. Action potentials were recorded as a current in voltage-clamp mode. To avoid phototoxicity, exposures to excitation lights were briefly used only to trace the axon and monitor the puffing area (see below). High-resolution images of whole axons were acquired after completion of the electrophysiology experiments. Exposure to the excitation lasers did not significantly affect
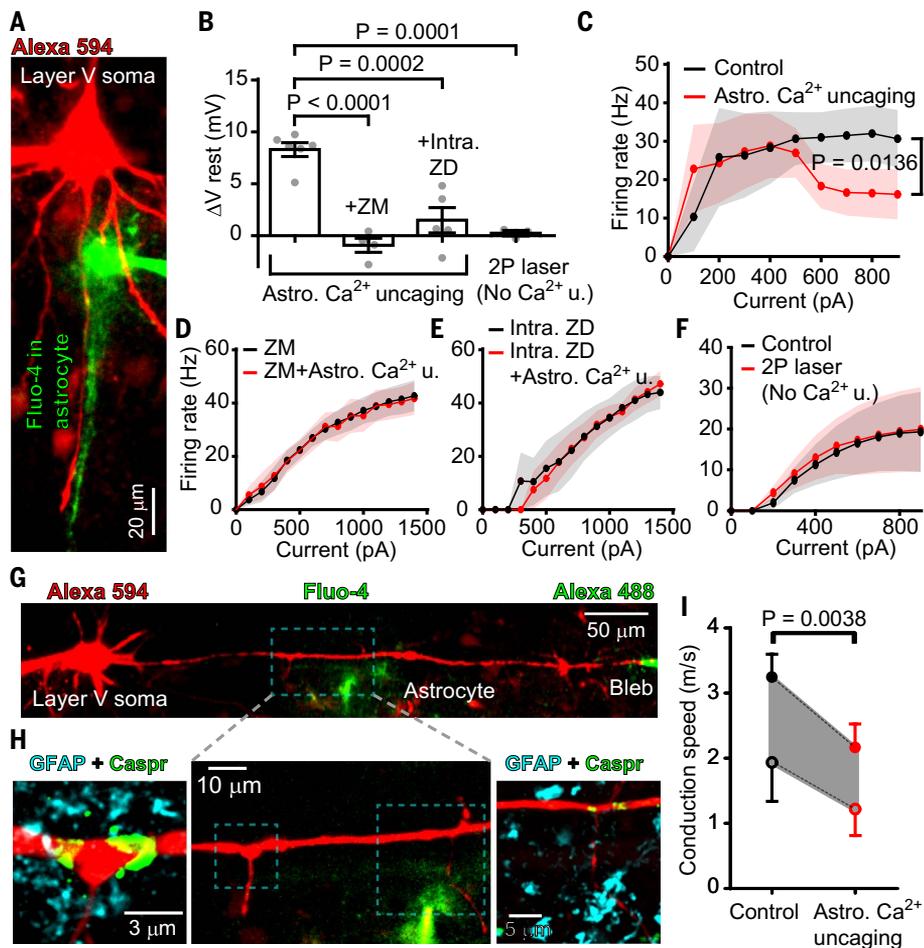
Fig. 6. Ca²⁺ concentration rises in astrocytes regulate pyramidal cell excitability and axonal conduction speed. (**A**) Patch-clamped L5 pyramidal neuron (with Alexa Fluor 594 in the left pipette, red) and a periaxonal astrocyte filled with the Ca²⁺ cage NP-EGTA and Fluo-4 (right pipette, green). $[Ca^{2+}]_i$ rises in astrocyte processes near the axon (see movie S3). (**B**) Resting potential (V_{rest}) depolarized after astrocyte Ca²⁺ uncaging but not when blocking $A_{2a}Rs$ with superfused ZM 241385 (100 nM) or I_h channels with ZD7288 (20 μM in the pipette) nor when two-photon laser excitation failed to raise $[Ca^{2+}]_i$ (No Ca²⁺ u.; see fig. S2) (Astro. Ca²⁺ uncaging: $n = 6$, +ZM: $n = 4$, +Intra. ZD: $n = 5$, 2P laser without uncaging: $n = 3$; one-way ANOVA, $P < 0.0001$). (**C**) Neuronal firing rate evoked by injecting 1 s current steps in 100 pA increments before (black) and after astrocytic Ca²⁺ uncaging (red). (**D** to **F**) As in (C) but with ZM 241385 [$n = 4$ (D)], or ZD7288 [$n = 4$ (E)], or with illumination that failed to uncage Ca²⁺ [$n = 3$ (F)]. (**G**) Live imaging of an L5 pyramidal neuron patch-clamped at the soma (left pipette, loading red Alexa Fluor 594) and the axon end (right pipette, green). A perinodal astrocyte (near axon branches) was patch-filled with NP-EGTA and Fluo-4. (**H**) Middle: high-resolution image of the dashed box in (G). Left and right images show the areas in the dashed boxes of the middle image after immunostaining for GFAP and Caspr. Nodes flanked by Caspr (green) are close to GFAP-positive astrocyte processes (cyan). (**I**) Estimated axonal conduction speed before and after astrocyte Ca²⁺ uncaging (see text associated with Fig. 4E for assumptions made). Data in (A) to (H) are from rats; (I) combines data from rats and mice (neither the initial speed nor the percentage change evoked by Ca²⁺ uncaging differed significantly between rats and mice, $P = 0.08$ and $P = 0.93$, respectively).

the waveform of action potentials. In Fig. 6, D and E, where the effects of adenosine receptors or HCN channels were blocked, there was no change in action potential width measured at the soma. For the first spike evoked by a 500-pA step, the full width at half-maximum with ZM 241385 was 1.15 ± 0.13 msec before and 1.18 ± 0.14 msec after Ca²⁺ uncaging ($n = 4$; not significantly different, $P = 0.12$); with ZD7288, it was 1.25 ± 0.17 msec before and

1.21 ± 0.13 msec after Ca²⁺ uncaging ($n = 4$; not significantly different, $P = 0.44$). Similarly, there was no difference in the action potential width measured at the bleb with ZD7288 inside the neurons (fig. S6A); the full width at half-maximum (the maximum being the amplitude of the inward current peak) was 0.53 ± 0.17 msec before and 0.53 ± 0.10 msec after Ca²⁺ uncaging ($n = 5$; not significantly different, $P = 0.99$). Microelectrodes with resistances of 8 to

9 MΩ were filled with aCSF and 100 μM Alexa Fluor 488 (ThermoFisher Scientific). Blebs were patch-clamped in cell-attached configuration, and the signals were filtered at 2 kHz and digitized at 50 kHz. Action potentials at the soma were evoked and recorded, and action currents at the axon bleb were recorded simultaneously. To accurately determine the delay between the somatic and axonal signals, at least 100 somatic spikes were evoked. First derivatives of the somatic and axonal signals were generated and then time-shifted to align the peaks of the somatic spikes. The signals were then averaged, and the soma-axon delay was measured as the difference between the onset of the axonal spike (time point recorded before a current drop of >0.5 pA/ms) and the somatic spike (time point recorded before an increase of >1 mV/ms).

Local application of drugs to axons

CGS 21680 (500 nM; Cayman Chemical) or 100 μM adenosine (Sigma-Aldrich) were puff-applied onto the AIS or nodes of Ranvier. The drugs were added to aCSF with 100 μM Alexa Fluor 594 to monitor the spread of the drugs. Two or three MΩ pipettes were filled with this solution and placed 10 μm away from the targeted axon. Positive pressure was either applied with a microinjector (PMI-100, Dagan) for 20 ms at 10 psi or controlled manually with a syringe. In both cases, positive pressure was calibrated and live monitored to eject drug over a radius of ≤20 μm (from the tip of the pipette set at saturating intensity to the edge of detectable fluorescence). The flow of the perfusion was set to wash out the puffed drug in the direction away from the targeted neuron. The AIS was detected by adding 100 μM Alexa Fluor 594 into the intracellular solution, and its diffusion into the axon was live monitored. The pipette puffing onto the AIS was placed near the distal AIS 25 to 30 μm away from the soma. The pipette puffing onto the nodes was placed near an axonal branch (detected from the Alexa Fluor 594 fill) or green fluorescent protein (GFP) signal detected along the axon of a Thy1-Caspr-GFP mouse. Caspr was post hoc immunolabeled to confirm the presence of nodes at the puffing sites.

Patch-clamping, calcium uncaging, and imaging of astrocytes

Astrocytes were detected by their morphology and with the selective marker sulforhodamine 101 (SR 101). Before the experiments, the slices were incubated with 1 μM SR101 (Tocris Bioscience) added to the slicing solution for 20 min at 37°C. The presence of astrocytes was confirmed by post hoc fixing slices and immunolabeling for GFAP. Microelectrodes with resistances of 7 to 8 MΩ were filled with a K-methylsulfate intracellular solution containing (in mM): 100 KMeSO₄, 50 KCl, 2 MgCl₂, 4 MgATP,

0.3 Na$_2$GTP, and 10 HEPES. Fluo-4 (100 µM; ThermoFisher Scientific) was added to image calcium changes, and 5 mM NP-EGTA (ThermoFisher Scientific) was added to allow uncaging of calcium in single astrocytes. Images were acquired at 2 Hz with a confocal argon laser, and NP-EGTA photolysis was obtained by applying two-photon excitation at 720 nm to the soma (10 iterations, 2.55 µs pixel dwell time). Laser intensity was set at 10 mW and, if needed, was increased gradually until a calcium concentration rise was evoked (fig. S2). Intensities just below those needed to evoke a detectable [Ca^{2+}]$_i$ rise were used as control experiments to check that two-photon illumination alone was not responsible for the release of ATP and adenosine generation observed. In the experiments examining calcium activity at astrocyte processes, images were acquired at the plane of the axon or of a dendrite contacting astrocyte processes. Regions of interest (ROIs) were selected and [Ca^{2+}]$_i$ changes were measured as $\Delta F/F$ after background subtraction. At the start of the experiments, the baseline astrocyte Ca^{2+} activity was recorded for 10 s, and, over this brief period, no spontaneous Ca^{2+} transients were observed.

Immunohistochemistry

Brains from Thy1-Caspr-GFP mice were perfusion-fixed in 4% paraformaldehyde (PFA) in 0.01 M phosphate-buffered saline (PBS), and fixed tissue was then cut into 70-µm-thick slices. Alternatively, 300-µm-thick acute slices from mouse and rat brains were immersion-fixed in a solution containing 4% PFA, 4% sucrose, and 0.1 M PBS. The slices were permeabilized with 0.2% Triton X-100 (Sigma-Aldrich) in a blocking solution (10% goat serum in 0.01 M PBS) for 1 hour. The slices were then incubated overnight at 4°C with the following primary antibodies, as required: rabbit anti-A$_{2a}$R (Abcam, ab3461, 1:100), mouse anti-A$_{2a}$R [Millipore, 05-717, which has been validated as giving no labeling in A$_{2a}$R KO tissue (40), 1:200], rabbit anti-A$_1$R (Abcam, ab82477, 1:100), rabbit anti-A$_{2b}$R (Cohesion, CPA3755, 1:100), mouse anti-Ankyrin G (Neuromab, N106/36, 1:500), mouse anti-panNav (Sigma-Aldrich, K58/35, 1:100), mouse anti-Caspr (Neuromab, K65/35, 1:100), chicken anti-GFP (Millipore, AB16901, 1:1000), rabbit anti-GFAP (Millipore, AB5804, 1:500), rabbit anti-HCN1 (Alomone, APC 056, 1:100), and rabbit anti-HCN2 (Alomone, APC 030, 1:100). The slices were then incubated for 2 hours at room temperature with the following secondary antibodies, as required (ThermoFisher Scientific, 1:500): anti-chicken or anti-mouse Alexa Fluor 488, anti-rabbit or anti-mouse Alexa Fluor 546, and anti-rabbit Alexa Fluor 647. The slices were incubated with 4′,6-diamidino-2-phenylindole nuclear stain (1:50,000 in PBS from a 5 mg/ml stock concentration) for 10 min

and mounted in Dako fluorescent mounting medium. Slices were washed with 0.01 M PBS three times with 10 min between each step. Negative control experiments were also performed to check for any labeling caused by unspecific binding of the secondary antibodies. For this, we followed the same protocol but omitted the incubation with the primary antibodies. Slices were imaged using a Zeiss LSM700 confocal microscope with a Zeiss Plan-Apochromat 63× oil immersion lens, and images were acquired with ZEN Microscope Software (Zeiss). Z-stacks of 1-µm intervals were imaged, and their maximum intensity was projected using ImageJ (FIJI). A line was drawn along the axons to plot intensity profiles. To plot node of Ranvier profiles, the width of the line was adjusted to fit the width of the Caspr-labeled paranodes. To analyze GFAP staining running parallel to axons, the width of the line was adjusted to 5 µm and centered on the axon.

Quantification of putative ATP-containing vesicles

Before the experiments, the slices were incubated with 20 µM quinacrine dihydrochloride (Sigma-Aldrich) added to the slicing solution for 25 min at 37°C. Quinacrine is a green selective marker for ATP-containing vesicles (7) or lysosomes (41). Calcium was uncaged and imaged from single astrocytes as described above using the red Ca^{2+} indicator Rhod-2 (50 µM, ThermoFisher Scientific) instead of Fluo-4. Images of astrocyte processes with ATP vesicles were acquired before and after Ca^{2+} uncaging with two-photon excitation at 720 nm at the soma. Adjacent areas were also imaged. ROIs located a similar distance away from the astrocyte soma but without any detectable dye-filled astrocyte processes within a 5 µm perimeter minimum were selected. With ImageJ, a constant threshold was applied to the images and particle analysis was used to quantify the number of ATP vesicles. The mean Feret's diameter of ATP vesicles was 0.56 ± 0.03 µm (n = 2227), similar to previous reports (42).

Detection of extracellular ATP

Changes in extracellular ATP level were detected with a luciferin/luciferase–based chemiluminescence assay emitting green light. Perfusion of brain slices was halted and 50-µl aliquots containing 12 mg/ml luciferin (Sigma-Aldrich) and 5 mg/ml luciferase (Sigma-Aldrich) were added to a 1-ml bath chamber filled with aCSF at room temperature (because luciferase is not stable at higher temperatures). Calcium was uncaged and imaged from single astrocytes as described above using the red Ca^{2+} indicator Rhod-2 (50 µM) instead of Fluo-4. A field of view containing an astrocyte and its processes was selected and ATP-derived bioluminescence was collected in darkness using

highly sensitive GaAsP detectors with a Zeiss LSM780 two-photon/confocal microscope.

Estimating axonal conduction velocity

We estimated axonal conduction velocities on the basis of parameters acquired experimentally from dual soma and axon bleb patch-clamp recordings, live confocal imaging, and post hoc immunostaining of layer V pyramidal neurons. In accordance with previous studies, two assumptions were made: (i) spikes initiate at the distal half of the AIS (the AIS being defined as being from the edge of the soma to the start of the first Caspr-labeled paranode) because in the distal AIS Na$^+$ channels are found in high density, have a low voltage threshold, and are isolated from the capacitive load of the soma (43, 44) and (ii) forward conduction speed is two to three times faster than backward conduction speed because of the lower Na$^+$ channel density in the proximal AIS and the capacitive load of the soma (16, 44). The axonal conduction speed can be then calculated as follows:

$$v = \frac{x_{\text{bleb}} - 2x_{\text{soma}}}{T} \text{ or } v = \frac{x_{\text{bleb}} - 3x_{\text{soma}}}{T} \quad (3)$$

where v is the speed from the spike initiation site to the axon bleb, T is the delay time from the somatic signal to the bleb signal (obtained from dual patch-clamp recordings), and x_{bleb} and x_{soma} are the distances from the spike initiation site to the recording sites on the axon bleb or on the soma, respectively (obtained from confocal imaging by assuming a position for spike initiation).

Computer simulations of infinite corpus callosal axon

As in our previous studies (17, 45, 46), action potential conduction along myelinated axons was simulated using MATLAB. Electrophysiological parameters were based on the finite impedance double-cable model (model C) of Richardson et al. (47), except that the membrane capacitance was taken as the physiologically measured value of 0.9 µF/cm^2 (48). The differential equations of the model were derived and solved as in the myelinated axon model of Halter and Clark (49), in which the axon is divided into compartments representing the node, paranode, and internode. The MATLAB code, including all parameters and equations, is available (see the Acknowledgments). Conduction speed simulations of long callosal-like axons were performed as described previously (17), where the parameters used were based on experimental data. The speed was measured between nodes 20 and 30 in a uniform axon containing 51 nodes and 50 internodes of constant lengths (nodes: 1.5 µm, internodes: 81.7 µm) and diameters (nodes: 0.64 µm, internodes: 0.73 µm). The periaxonal space thickness, which has an

important effect on conduction speed (17, 50), was set at 15 nm except in the paranodes (the 1.9-µm end parts of the internodes), where the width was reduced to 0.0123 nm (17). Assuming a myelin wrap periodicity of 15.6 nm, five myelin wraps were needed to set the g-ratio close to 0.8. Each node expressed fast voltage-gated Na^+ (Na_V) channels, persistent Na_V channels, and slow voltage-gated potassium (K_V) channels at fully activated conductance densities of 10, 0.01, and 0.4 mS/mm^2, respectively, as well as adenosine-gated I_h channels at a density of either 0 (for no $A_{2a}R$ activation) or 0.1565 (to mimic $A_{2a}R$ activation) mS/mm^2. This density was experimentally derived as follows: the maximum I_h conductance (derived from tail current analysis as in Fig. 3, I and J) evoked in the ~10-µm length of the distal AIS was divided by the area of the distal AIS to obtain a fully-activated conductance density of 0.111 mS/mm^2. Immunohistochemical labeling of $A_{2a}Rs$ then showed their density at nodes of Ranvier to be a factor of 1.41 higher than in the distal AIS (calculated by integrating the background-subtracted fluorescent signal across a small length w of the axon and dividing by $\pi \cdot w \cdot d$, where d is the diameter of the axon), implying a density at the nodes of 0.1565 mS/mm^2. The node resting potential in the absence of adenosine was set to –82 mV by adjusting the magnitude of a leak conductance (to 0.113 mS/mm^2) with a reversal potential of –84 mV (the reversal potential of the other K^+ currents in the model). The leak current represents K^+ leak channels such as TRAAK present in the nodes of Ranvier (51, 52).

Computer simulations of patch-clamped neuron with soma, AIS, and three internodes

This model was then modified so that the dimensions of a specimen patch-clamped and imaged neuron acquired for the present study (Fig. 4) were implemented (Fig. 5A). The model included "nodes" representing the soma, the proximal AIS, the distal AIS, three nodes of Ranvier, and a terminating bleb. To represent the area and thus the capacitance of the real soma, the diameter and length of the cylindrical "node" representing the soma were both set to 18 µm. The proximal and distal AIS had lengths of 21.9 and 10 µm, respectively, and diameters (measured experimentally as the average over each of these two zones) of 1.046 and 0.525 µm respectively. The soma and proximal AIS, and the proximal and distal AIS, were separated by extremely small (10^{-7} µm long) "internodes" (which are essential for the alternating node-internode model to function in MATLAB; not shown in Fig. 5A) with diameters of 1.046 and 0.79 µm, respectively. Distal to the AIS are three internodes of lengths 24.91, 52.44, and 39.20 µm and diameters of 0.51, 0.56, and 0.53 µm respectively, each followed by nodes of Ranvier of lengths 1.126,

0.915, and 0.414 µm, and diameters of 0.445, 0.452, and 0.401 µm, respectively. The third node of Ranvier was followed by an extremely small (10^{-7} µm long) "internode" of diameter 0.4 µm and then a terminal bleb of length 1.64 µm and diameter 3 µm. Each node of Ranvier expressed the same conductance as in the infinite cable model. The proximal and distal AIS compartments expressed fast Na_V, persistent Na_V, and slow K_V channels at the same densities as in the infinite cable model, and in addition a low threshold K_V channel with a maximum conductance of 0.4 mS/mm^2, which was needed to allow the generation of repetitive action potential trains in response to current injected at the soma. Adenosine-insensitive I_h conductance (with a half-maximum activation voltage of –103.5 mV, as found on average in experiments as in Fig. 3J) was expressed in the soma and proximal AIS (as seen immunohistochemically for HCN1 channels) at a density of 0.0033 mS/mm^2 (set so as to reproduce the mean I_h maximal conductance seen in the absence of adenosine in Fig. 3, I and J), whereas adenosine-sensitive I_h was present in the distal AIS at a density of 0.111 mS/mm^2 and in the nodes of Ranvier at a density 1.41-fold higher (see above). The density used for the distal AIS was set to increase the maximum I_h conductance measured at the soma by 51% as observed during activation of $A_{2a}Rs$ in the distal AIS (Fig. 3, I and J), and the midpoint of its activation curve was at –80 mV to reproduce the positive shift for the total I_h apparent activation curve in Fig. 3J. The terminal bleb expressed no voltage-gated conductances. To match the model to the experimental data, we wanted to reproduce the 5.8-mV depolarization recorded at the soma when puffed adenosine activated I_h in the distal AIS (Fig. 3E). We found that if we set the resting potential to –82 mV in the soma and AIS using a leak conductance with a reversal potential of –84 mV (as in the nodes), then this introduced too much resting conductance, reducing the depolarization evoked at the soma when $A_{2a}Rs$ were activated in the distal AIS to only +1.55 mV. Accordingly, in the soma, AIS, and terminal bleb, we used a nominal leak reversal potential of –4000 mV, converting the leak into an essentially voltage-independent (~zero conductance) current, similar conceptually to the constant outward current generated by the Na^+/K^+ pump. The adenosine-sensitive I_h (when activated in the distal AIS) then generated a depolarization of 5.9 mV at the soma. To investigate the effect of the adenosine-evoked I_h current, the action potential speed was measured between the first and the last nodes of Ranvier when current was injected briefly (1 nA for 100 µsec) at the soma. The model reproduced reasonably well the assumptions that we made to assess the conduction speed in our experiments: In

the simulations, spikes evoked by current injection at the soma were initiated in the distal AIS "node", the forward conduction speed was faster than the backward speed (from distal AIS to bleb: 1.33 m/s; from distal AIS to soma: 0.23 m/s), and the conduction speed from the distal AIS to the bleb (1.33 m/s) was in the range estimated from the experiments in Figs. 4E and 6I (1.31 to 2.23 m/s).

Code availability

The computer code used for the simulations described above has been deposited in Zenodo (53).

Statistics

Statistical analyses and graphs were performed with GraphPad Prism 6. Data are presented as mean ± SEM. Data normality was assessed with D'Agostino & Pearson omnibus or Kolmogorov-Smirnov tests. Comparisons of normally distributed two groups were made using two-tailed Student t tests. When treatments involved more than two independent groups, statistical comparisons were performed with one-way ANOVA and post hoc Tukey's multiple comparisons. Data that were not normally distributed were analyzed with Mann-Whitney test or Wilcoxon matched-pairs signed rank test. Assessment of whether the slope of linear regressions differed significantly from zero was obtained using the t statistic for the slope. P values within any figure panel were adjusted for multiple comparisons.

Gender and species effects

Mice were used in experiments when it was essential to have the nodes labeled with Caspr-GFP. Rats were also used because they are more generally available at all ages in our university. We observed no differences between the two species, for example, in

(i) the presence of $A_{2a}Rs$ and HCN channels at nodes of Ranvier and the AIS;

(ii) the initial speed and the percentage change evoked by CGS 21680 puff onto nodes, which did not differ significantly between rats and mice ($P = 0.43$ and $P = 0.15$, respectively); and

(iii) the initial speed and the percentage change evoked by Ca^{2+} uncaging in perinodal astrocytes, which did not differ significantly between rats and mice ($P = 0.08$ and $P = 0.93$, respectively).

Animals of both sexes were used because of increasing awareness of the fact that gender can play a role in determining function. For major results, we found no differences between the two sexes, for example, in

(i) the presence of $A_{2a}Rs$ and HCN channels at nodes of Ranvier and the AIS;

(ii) the initial resting membrane potential and the change evoked by CGS 21680 puff onto the AIS, which did not differ significantly

between males and females (P = 0.69 and 0.75 respectively); and

(iii) the initial speed and the percentage change evoked by CGS 21680 puff onto nodes, which did not differ significantly between males and females (P = 0.3 and P = 0.45, respectively).

REFERENCES AND NOTES

1. N. J. Allen, Astrocyte regulation of synaptic behavior. *Annu. Rev. Cell Dev. Biol.* **30**, 439–463 (2014). doi: 10.1146/annurev-cellbio-100913-013053; pmid: 25288116

2. M. H. P. Kole *et al.*, Action potential generation requires a high sodium channel density in the axon initial segment. *Nat. Neurosci.* **11**, 178–186 (2008). doi: 10.1038/nn2040; pmid: 18204443

3. V. A. Larson *et al.*, Oligodendrocytes control potassium accumulation in white matter and seizure susceptibility. *eLife* **7**, e34829 (2018). doi: 10.7554/eLife.34829; pmid: 29596047

4. A. S. Saab, I. D. Tzvetanova, K.-A. Nave, The role of myelin and oligodendrocytes in axonal energy metabolism. *Curr. Opin. Neurobiol.* **23**, 1065–1072 (2013). doi: 10.1016/j.conb.2013.09.008; pmid: 24094633

5. C. Ffrench-Constant, R. H. Miller, J. Kruse, M. Schachner, M. C. Raff, Molecular specialization of astrocyte processes at nodes of Ranvier in rat optic nerve. *J. Cell Biol.* **102**, 844–852 (1986). doi: 10.1083/jcb.102.3.844; pmid: 2419343

6. A. Araque *et al.*, Gliotransmitters travel in time and space. *Neuron* **81**, 728–739 (2014). doi: 10.1016/j.neuron.2014.02.007; pmid: 24559669

7. S. Forveille *et al.*, Quinacrine-mediated detection of intracellular ATP. *Methods Enzymol.* **629**, 103–113 (2019). doi: 10.1016/bs.mie.2019.05.050; pmid: 31727236

8. T. Pfeiffer, D. Attwell, Brain's immune cells put the brakes on neurons. *Nature* **586**, 366–367 (2020). doi: 10.1038/d41586-020-02713-7; pmid: 32999439

9. K. Baalman *et al.*, Axon initial segment-associated microglia. *J. Neurosci.* **35**, 2283–2292 (2015). doi: 10.1523/JNEUROSCI.3751-14.2015; pmid: 25653382

10. J. Zhang, X. Yang, Y. Zhou, H. Fox, H. Xiong, Direct contacts of microglia on myelin sheath and Ranvier's node in the corpus callosum in rats. *J. Biomed. Res.* **33**, 192–200 (2019). pmid: 30403198

11. D. DiFrancesco, P. Tortora, Direct activation of cardiac pacemaker channels by intracellular cyclic AMP. *Nature* **351**, 145–147 (1991). doi: 10.1038/351145a0; pmid: 1709448

12. G. Vargas, M. T. Lucero, Dopamine modulates inwardly rectifying hyperpolarization-activated current (I_h) in cultured rat olfactory receptor neurons. *J. Neurophysiol.* **81**, 149–158 (1999). doi: 10.1152/jn.1999.81.1.149; pmid: 9914276

13. N. Byczkowicz *et al.*, HCN channel-mediated neuromodulation can control action potential velocity and fidelity in central axons. *eLife* **8**, e42766 (2019). doi: 10.7554/eLife.42766; pmid: 31496517

14. F. C. Roth, H. Hu, An axon-specific expression of HCN channels catalyzes fast action potential signaling in GABAergic interneurons. *Nat. Commun.* **11**, 2248 (2020). doi: 10.1038/s41467-020-15791-y; pmid: 32382046

15. K. W. Ko, M. N. Rasband, V. Meseguer, R. H. Kramer, N. L. Golding, Serotonin modulates spike probability in the axon initial segment through HCN channels. *Nat. Neurosci.* **19**, 826–834 (2016). doi: 10.1038/nn.4293; pmid: 27110919

16. Y. Yu, Y. Shu, D. A. McCormick, Cortical action potential backpropagation explains spike threshold variability and rapid-onset kinetics. *J. Neurosci.* **28**, 7260–7272 (2008). doi: 10.1523/JNEUROSCI.1613-08.2008; pmid: 18632930

17. I. L. Arancibia-Cárcamo *et al.*, Node of Ranvier length as a potential regulator of myelinated axon conduction speed. *eLife* **6**, e23329 (2017). doi: 10.7554/eLife.23329; pmid: 28130923

18. A. Lörincz, T. Notomi, G. Tamás, R. Shigemoto, Z. Nusser, Polarized and compartment-dependent distribution of HCN1 in pyramidal cell dendrites. *Nat. Neurosci.* **5**, 1185–1193 (2002). doi: 10.1038/nn962; pmid: 12389030

19. B. J. Wainger, M. DeGennaro, B. Santoro, S. A. Siegelbaum, G. R. Tibbs, Molecular mechanism of cAMP modulation of HCN pacemaker channels. *Nature* **411**, 805–810 (2001). doi: 10.1038/35081088; pmid: 11459060

20. N. B. Hamilton, D. Attwell, Do astrocytes really exocytose neurotransmitters? *Nat. Rev. Neurosci.* **11**, 227–238 (2010). doi: 10.1038/nrn2803; pmid: 20300101

21. B. S. Khakh, Astrocyte-neuron interactions in the striatum: Insights on identity, form, and function. *Trends Neurosci.* **42**, 617–630 (2019). doi: 10.1016/j.tins.2019.06.003; pmid: 31351745

22. N. Hamilton *et al.*, Mechanisms of ATP- and glutamate-mediated calcium signaling in white matter astrocytes. *Glia* **56**, 734–749 (2008). doi: 10.1002/glia.20649; pmid: 18293404

23. A. Natsubori *et al.*, Intracellular ATP levels in mouse cortical excitatory neurons varies with sleep-wake states. *Commun. Biol.* **3**, 491 (2020). doi: 10.1038/s42003-020-01215-6; pmid: 32895482

24. T. Porkka-Heiskanen *et al.*, Adenosine: A mediator of the sleep-inducing effects of prolonged wakefulness. *Science* **276**, 1265–1268 (1997). doi: 10.1126/science.276.5316.1265; pmid: 9157887

25. M. M. Halassa *et al.*, Astrocytic modulation of sleep homeostasis and cognitive consequences of sleep loss. *Neuron* **61**, 213–219 (2009). doi: 10.1016/j.neuron.2008.11.024; pmid: 19186164

26. L. I. Schmitt, R. E. Sims, N. Dale, P. G. Haydon, Wakefulness affects synaptic and network activity by increasing extracellular astrocyte-derived adenosine. *J. Neurosci.* **32**, 4417–4425 (2012). doi: 10.1523/JNEUROSCI.5689-11.2012; pmid: 22457491

27. Z. L. Huang *et al.*, Adenosine A2A, but not A1, receptors mediate the arousal effect of caffeine. *Nat. Neurosci.* **8**, 858–859 (2005). doi: 10.1038/nn1491; pmid: 15965471

28. W. Wefelmeyer, D. Cattaert, J. Burrone, Activity-dependent mismatch between axo-axonic synapses and the axon initial segment controls neuronal output. *Proc. Natl. Acad. Sci. U.S.A.* **112**, 9757–9762 (2015). doi: 10.1073/pnas.1502902112; pmid: 26195803

29. K. J. Bender, C. P. Ford, L. O. Trussell, Dopaminergic modulation of axon initial segment calcium channels regulates action potential initiation. *Neuron* **68**, 500–511 (2010). doi: 10.1016/j.neuron.2010.09.026; pmid: 21040850

30. P. König, A. K. Engel, W. Singer, Integrator or coincidence detector? The role of the cortical neuron revisited. *Trends Neurosci.* **19**, 130–137 (1996). doi: 10.1016/S0166-2236(96)80019-1; pmid: 8658595

31. E. Salinas, T. J. Sejnowski, Correlated neuronal activity and the flow of neural information. *Nat. Rev. Neurosci.* **2**, 539–550 (2001). doi: 10.1038/35086012; pmid: 11483997

32. C. Adaikkan, L.-H. Tsai, Gamma entrainment: Impact on neurocircuits, glia, and therapeutic opportunities. *Trends Neurosci.* **43**, 24–41 (2020). doi: 10.1016/j.tins.2019.11.001; pmid: 31836315

33. S. Pajevic, P. J. Basser, R. D. Fields, Role of myelin plasticity in oscillations and synchrony of neuronal activity. *Neuroscience* **276**, 135–147 (2014). doi: 10.1016/j.neuroscience.2013.11.007; pmid: 24291730

34. C. Ledent *et al.*, Aggressiveness, hypoalgesia and high blood pressure in mice lacking the adenosine A_{2a} receptor. *Nature* **388**, 674–678 (1997). doi: 10.1038/41771; pmid: 9262401

35. M. P. Kaster *et al.*, Caffeine acts through neuronal adenosine A_{2A} receptors to prevent mood and memory dysfunction triggered by chronic stress. *Proc. Natl. Acad. Sci. U.S.A.* **112**, 7833–7838 (2015). doi: 10.1073/pnas.1423088112; pmid: 26056314

36. Y.-J. Liu *et al.*, Research progress on adenosine in central nervous system diseases. *CNS Neurosci. Ther.* **25**, 899–910 (2019). doi: 10.1111/cns.13190; pmid: 31334608

37. D. J. Hines, P. G. Haydon, Astrocytic adenosine: From synapses to psychiatric disorders. *Philos. Trans. R. Soc. Lond. B Biol. Sci.* **369**, 20130594 (2014). doi: 10.1098/rstb.2013.0594; pmid: 25225088

38. V. Brivio, C. Faivre-Sarrailh, E. Peles, D. L. Sherman, P. J. Brophy, Assembly of CNS nodes of Ranvier in myelinated nerves is promoted by the axon cytoskeleton. *Curr. Biol.* **27**, 1068–1073 (2017). doi: 10.1016/j.cub.2017.01.025; pmid: 28318976

39. Y. Shu, A. Hasenstaub, A. Duque, Y. Yu, D. A. McCormick, Modulation of intracortical synaptic potentials by presynaptic somatic membrane potential. *Nature* **441**, 761–765 (2006). doi: 10.1038/nature04720; pmid: 16625207

40. A. G. Orr *et al.*, Astrocytic adenosine receptor A_{2A} and G_s-coupled signaling regulate memory. *Nat. Neurosci.* **18**, 423–434 (2015). doi: 10.1038/nn.3930; pmid: 25622143

41. Z. Zhang *et al.*, Regulated ATP release from astrocytes through lysosome exocytosis. *Nat. Cell Biol.* **9**, 945–953 (2007). doi: 10.1038/ncb1620; pmid: 17618272

42. C. Cserép *et al.*, Microglia monitor and protect neuronal function through specialized somatic purinergic junctions. *Science* **367**, 528–537 (2020). doi: 10.1126/science.aax6752; pmid: 31831638

43. W. Hu *et al.*, Distinct contributions of Na(v)1.6 and Na(v)1.2 in action potential initiation and backpropagation. *Nat. Neurosci.* **12**, 996–1002 (2009). doi: 10.1038/nn.2359; pmid: 19633666

44. G. Baranauskas, Y. David, I. A. Fleidervish, Spatial mismatch between the Na$^+$ flux and spike initiation in axon initial segment. *Proc. Natl. Acad. Sci. U.S.A.* **110**, 4051–4056 (2013). doi: 10.1073/pnas.1215125110; pmid: 23341597

45. M. C. Ford *et al.*, Tuning of Ranvier node and internode properties in myelinated axons to adjust action potential timing. *Nat. Commun.* **6**, 8073 (2015). doi: 10.1038/ncomms9073; pmid: 26305015

46. Y. Bakiri, R. Káradóttir, L. Cossell, D. Attwell, Morphological and electrical properties of oligodendrocytes in the white matter of the corpus callosum and cerebellum. *J. Physiol.* **589**, 559–573 (2011). doi: 10.1113/jphysiol.2010.201376; pmid: 21098009

47. A. G. Richardson, C. C. McIntyre, W. M. Grill, Modelling the effects of electric fields on nerve fibres: Influence of the myelin sheath. *Med. Biol. Eng. Comput.* **38**, 438–446 (2000). doi: 10.1007/BF02345014; pmid: 10984943

48. L. J. Gentet, G. J. Stuart, J. D. Clements, Direct measurement of specific membrane capacitance in neurons. *Biophys. J.* **79**, 314–320 (2000). doi: 10.1016/S0006-3495(00)76293-X; pmid: 10866957

49. J. A. Halter, J. W. Clark Jr., A distributed-parameter model of the myelinated nerve fiber. *J. Theor. Biol.* **148**, 345–382 (1991). doi: 10.1016/S0022-5193(05)80242-5; pmid: 2016898

50. K. M. Young *et al.*, Oligodendrocyte dynamics in the healthy adult CNS: Evidence for myelin remodeling. *Neuron* **77**, 873–885 (2013). doi: 10.1016/j.neuron.2013.01.006; pmid: 23473318

51. H. Kanda *et al.*, TREK-1 and TRAAK are principal K$^+$ channels at the nodes of Ranvier for rapid action potential conduction on mammalian myelinated afferent nerves. *Neuron* **104**, 960–971.e7 (2019). doi: 10.1016/j.neuron.2019.08.042; pmid: 31630908

52. S. G. Brohawn *et al.*, The mechanosensitive ion channel TRAAK is localized to the mammalian node of Ranvier. *eLife* **8**, e50403 (2019). doi: 10.7554/eLife.50403; pmid: 31674909

53. Code used in the simulations for: J. Lezmy, I. L. Arancibia-Cárcamo, T. Quintela-López, D. L. Sherman, P. J. Brophy, D. Attwell, Astrocyte Ca^{2+}-evoked ATP release regulates myelinated axon excitability and conduction speed, Zenodo (2021); doi: 10.5281/zenodo.5177076

54. Code used to simulate the action potential in myelinated axons for: J. Lezmy, I. L. Arancibia-Cárcamo, T. Quintela-López, D. L. Sherman, P. J. Brophy, D. Attwell, Astrocyte Ca^{2+}-evoked ATP release regulates myelinated axon excitability and conduction speed, Github (2021); https://github.com/AttwellLab/MyelinatedAxonModel.

Science

Astrocyte Ca-evoked ATP release regulates myelinated axon excitability and conduction speed

Jonathan LezmyI. Lorena Arancibia-CárcamoTania Quintela-LópezDiane L. ShermanPeter J. BrophyDavid Attwell

Glia control white matter information flow

The myelinated axons of the white matter mediate rapid information transmission between the brain's processing nodes. Axonal excitability and conduction speed are key determinants of neural circuit function, but it is largely unknown how they are regulated. Lezmy *et al.* examined the effects of adenosine on the functional properties of myelinated axons. They observed activity-dependent calcium rise in astrocyte processes, calcium-triggered ATP release from astrocytes, activation of adenosine receptors in the axon initial segment and the nodes of Ranvier, increased cyclic AMP concentration, activation of HCN2 channels, and depolarization of axons by 5 to 10 millivolts. This molecular pathway enabled astrocytes to increase the excitability of pyramidal neurons and to profoundly decrease the axonal conduction velocity. Astrocytes thus control signaling speed in myelinated axons. —PRS

View the article online
https://www.science.org/doi/10.1126/science.abh2858
Permissions
https://www.science.org/help/reprints-and-permissions

Use of think article is subject to the Terms of service